LAWRENCE
LIVERMORE
NATIONAL
LABORATORY

LLNL-JRNL-607773

Integrated Diagnostic Analysis of ICF Capsule Performance

C. Cerjan, P. T. Springer, S. A. Sepke

December 11, 2012

Physics of Plasmas

Disclaimer

Integrated diagnostic analysis of ICF capsule performance

Charles Cerjan, Paul T. Springer, and Scott A. Sepke

Lawrence Livermore National Laboratory 7000 East Avenue, Livermore, CA 94550

(Dated: November 28, 2012)

Abstract

A simple conceptual model is developed for typical Inertial Confinement Fusion (ICF) implosion conditions that integrates available diagnostic information to determine the stagnation properties of the interior fill and surrounding shell. Assuming pressure equilibrium at peak compression and invoking simple radiative and equation-of-state relations, the pressure, density and electron temperature are obtained by optimized fitting of the experimental output to simple, global functional forms. Typical observational data that may be used includes x-ray self-emission, directional neutron time-of-flight signals, neutron yield, high-resolution x-ray spectra and radiographic images. This approach has been validated by comparison with radiation-hydrodynamic simulations, producing semi-quantitative agreement. Model results implicate poor kinetic energy coupling to the hot core as the primary cause of the observed low thermonuclear burn yields.

I. INTRODUCTION

An understanding of the dynamics of imploding Inertial Confinement Fusion (ICF) capsules is crucial for a successful experimental program dedicated to achieving high convergence and gain. The relative roles of laser irradiation, hohlraum drive, and capsule response are all important and will be difficult to disentangle unless appropriate diagnostic probes are fielded and their results correlated. In the case of capsule implosions, several currently deployed diagnostics provide important information about the size and shape of the developing hot spot through x-ray self-emission, neutron production and average ion temperature by neutron time-of-flight signals, shell material mix into the hot spot by high-resolution x-ray spectra, and remaining mass during convergent ablation by x-ray backlighting. Obtaining a physically consistent picture of the implosion dynamics requires an integration of these disparate experimental data.

A simple model has been developed to address this integration that focuses on the characterization of the implosion process at peak energy production based on the assumption of pressure equilibrium at stagnation[1]. The corresponding density and electron temperature can be obtained from the hydrogenic equation-of-state, producing a relatively complete characterization of the implosion at this time. These quantities are simultaneously adjusted to match the experimental x-ray self-emission images and to evaluate neutron production and an average ion temperature. Once consistency is obtained, many important secondary quantities can be derived such as the fuel areal density, energy loss by radiative cooling or thermal conduction, neutron images and directional neutron spectra.

Application of this model to the extant implosion database has uncovered a substantial energy deficit in the conversion of the kinetic energy of the shell to work being done on the hot core compared to radiation-hydrodynamic simulaton. That is, model predictions of the hot core pressure and volume routinely show factors of two to four lower pressure, P, and volume, V, so the energy content of the hot core, $\frac{3}{2}PV$, is always lower than that obtained from simulation. The plot in Figure 1 displays this energy deficit for the cryogenic DT-filled implosion experiments to date. The poor transfer of kinetic energy to the hot core could explain the relatively large discrepancy between the experimental and simulated yields observed for these implosion experiments as graphically depicted in Figure 2.

Furthermore, low mode asymmetries in the assembled fuel layer are found to be con-

sistent with the optimized fits produced by the model. The constraints imposed by the directional neutron diagnostics upon the fit to the shell density reveal anisotropic mass distributions, typically more mass along the symmetry axis and skewing along the equator. The relationship of these noted asymmetries to the energy deficit is presently unclear .

In the following, this model will be more completely described. The assumed physical and mathematical basis for this fitting procedure will be presented in the next section. Validation of the model against radiation-hydrodynamic simulations appears in the second section; applications to available National Ignition Campaign data from several recent shots are presented in the third section. The last section details both immediate and longer term extensions of this approach.

II. MODEL BACKGROUND

The underlying physical basis of the proposed model relies on a simple model of the implosion characteristics at peak burn and the observation that most of the diagnostic information about the implosion describes the stagnation phase of the implosion. Specifically, the stagnating hot core is assumed to be in pressure equilibrium so that the electron density and temperature may be straightforwardly evaluated from a hydrogenic equation-of-state at any spatial location in this region. Since high energy x-ray self-emission essentially depends upon the square of the electron density and has a power law dependence in electron temperature[2], x-ray images along different lines-of-sight may then be reconstructed. The size of these experimental images essentially determines the volume of the core region. Similarly, analytic fits to light ion thermonuclear fusion rates are well-known from stellar astrophysical research[3]. These fits depend only upon density and temperature so, again, neutron production at any point in the hot spot may be evaluated. These derived data are then fit in the least squares sense to the available experimental data to obtain a self-consistent description of the core region at peak burn that includes the pressure and the spatially dependent density and temperature.

With direct imaging, such as Compton radiography, the characteristics of the cold, high density shell could be directly constrained in this framework. Since this type of back-lit image is not currently available, several indirect arguments can be invoked to deduce shell characteristics. First, the assembled fuel adiabat, which is proportional to $\frac{P}{\rho^{\gamma}}$, is assumed

to be 1.5. This value is consistent with estimates from VISAR shock-timing experiments. Second, the ratio of neutron production in the energy range 10-12 MeV to 13-15 MeV, the so-called DSR (Down Scattered Ratio), is directly proportional to the cold fuel areal density[4], providing another constraint on the assembled fuel. Comparison of the DSR values from the four neutron time-of-flight measurements currently at different chamber wall locations produces estimates of low-mode asymmetry in the shell. That is, differences in the DSR reflect asymmetric variations in the fuel areal density which can be generally described by low mode spherical harmonic functions included in the iterative fitting procedure.

The mathematical implementation of these ideas is straightforward. First, a three dimensional global fitting function to the density, ρ, is chosen to have separate contributions from the shell density, ρ_{sh}, and the hot core density, ρ_{hs}, where

$$\rho_{sh}\left(r,\theta,\phi\right)=\frac{\rho_{rsh}\left(\theta,\phi\right)}{\sigma\left(\theta,\phi\right)\sqrt{2\pi}}\exp\left[-\frac{\left(r-r_0\left(\theta,\phi\right)\right)^2}{2\sigma^2\left(\theta,\phi\right)}\right], \tag{1}$$

and

$$\rho_{hs}\left(r,\theta,\phi\right)=a_1+a_2\left(\frac{2r^2}{r_0\left(\theta,\phi\right)}\right)\left(1-\tanh\left(\frac{r}{r_0\left(\theta,\phi\right)}\right)^8\right), \tag{2}$$

where $a_1$and a_2 are fitting parameters and (r,θ,ϕ) are spherical co-ordinates. Qualitatively, the shell mass is described as a Gaussian exponential with angularly dependent width and position while the core region appears as a truncated shallow basin. The total density is a smooth combination of these two functional choices

$$\rho\left(r,\theta,\phi\right)=\left(\rho_{sh}\left(r,\theta,\phi\right)^2+\rho_{hs}\left(r,\theta,\phi\right)^2\right)^{\frac{1}{2}}. \tag{3}$$

The angular dependence appears in the several auxillary functions as expansions in terms of the normalized spherical harmonics, $Y_{lm}\left(\theta,\phi\right)$, which also contain fitting parameters b_{lm}, c_{lm},and d_{lm}

$$\rho_{rsh}\left(\theta,\phi\right)=\sum_{l,m}^{N_1,M_1}b_{lm}Y_{lm}\left(\theta,\phi\right), \tag{4}$$

$$r_0\left(\theta,\phi\right)=\sum_{l,m}^{N_2,M_2}c_{lm}Y_{lm}\left(\theta,\phi\right), \tag{5}$$

and

$$\sigma\left(\theta,\phi\right)=\sum_{l,m}^{N_3,M_3}d_{lm}Y_{lm}\left(\theta,\phi\right). \tag{6}$$

Second, the temperature is calculated by a fit to the THD equation-of-state from SESAME[5]

$$T\left(r,\theta,\phi\right)=1.306\frac{P}{\rho}\left(1-1.766\times10^{-4}\frac{\rho^{2.239}}{P^{1.300}}\right)^{0.769} \tag{7}$$

where the total pressure, P, is a fitting parameter with the units of Gbars. The critical assumption of pressure equilibrium appears explicitly in this evaluation. With these thermodynamic quantities in hand, the x-ray self-emission and neutron production may be calculated for different lines-of-sight along with the total neutron production in the core. These latter determinations provide the direct link to experimental data which will yield the complete set of parameters for a consistent global fit.

More specifically, the fit proceeds in the following manner. Two views of the x-ray self-emission are typically available: the Gated X-ray Dectector (GXD) image viewed from the waist of the hohlraum and the hardened Gated X-ray Imager (hGXI) image viewed from the pole. The corresponding synthetic images in the fitting procedure are generated by two ray-traces in the appropriate orientation using the opacity, κ, in the form

$$\kappa(r,\theta,\phi,E)=2.2\rho/(2.5^2E^{3.3}), \tag{8}$$

where E is the x-ray energy in keV. The emission is then obtained from

$$\varepsilon(r,\theta,\phi,E)=5.404\times10^{15}\rho\kappa\frac{E^3}{\left(\exp\left(E/T\right)-1\right)} \tag{9}$$

and

$$I_{xr}\left(x,y\right)=\int_{path}\varepsilon(z,E)\exp\left(-\kappa\left(z\right)\rho\left(z\right)\right)dz \tag{10}$$

for the image in the object plane, where both the waist and pole self-emission are evaluated, $I_w\left(x,y\right)$ and $I_p\left(x,y\right)$, typically on a relatively coarse grid with 5×5 μm pixel area. In the absence of absolutely calibrated x-ray images, two fitting parameters multiply each image separately to match the experimental scales. Note that if more self-emission or back-lit x-ray images were available, say at higher energy or different spatial locations, this information could be similarly incorporated into the fitting procedure.

Thermonuclear processes during the capsule implosion phase are routinely monitored by Neutron Time-Of-Flight (NTOF) signals that provide an estimate of the burn-averaged ion temperature from thermal broadening at peak neutron energy and by Nuclear Activation Diagnostic (NAD) foils that measure neutron yields above specific threshold values. Although

the neutron yield is a single number to be fit, the NTOF signal is collected as a voltage trace in time and must be fit at each temporal point. Both the yield and the NTOF signal are evaluated using analytic thermonuclear reactivities[3], $\sigma\bar{v}\,(cm^3/\sec)$, for d(d,n)^{3}He or d(t,n)^{4}He. (Note that other light ion reaction product fits are available, such as d(d,p)t, and could be fit to, say, an emitted proton spectrum.) Specifically, the number of neutrons produced, $n\,(r,\theta,\phi)$, is calculated on a relatively fine grid inside a large sphere

$$n\,(r,\theta,\phi) = n_1 n_2 \sigma\bar{v} t_b, \tag{11}$$

where the number of reacting species, $n_i (i = 1,2)$, is the known, loaded fraction of that element multiplied by Avogadro's number, the density, and divided by the atomic mass number, A, for a burn pulse duration, t_b,

$$n_i = \frac{n_f N_A \rho}{A}. \tag{12}$$

Note that t_b is experimentally determined from either the streaked x-ray images or from the Gamma Reaction History (GRH) diagnostic that monitors fusion gamma-rays. Energy dispersion of the neutrons is introduced by use of the Brysk formula[6] to obtain a neutron spectrum,n_{sp}, as a function of neutron energy, $E_n\,(keV)$,

$$n_{sp} = n\,(r,\theta,\phi,E_n)\exp\left[-\frac{(E_n - \langle E_n\rangle)^2}{m_f\,\langle E_n\rangle\,T_{ion}}\right], \tag{13}$$

where $\langle E_n\rangle$ is the thermally averaged kinetic energy and m_f is the appropriate mass factor for the selected thermonuclear reaction. Integrating the neutron production over the sphere now produces the neutron yield for the specified reaction which is fit to the experimentally determined neutron yield. The energy-dispersed neutron spectrum is further processed by an instrumental response function converting the spectrum into a voltage trace. The predicted voltage signal is then fit to the NTOF trace at each time point. After a successful fit, the full width at half maximum of the energy-dispersed neutron spectrum provides an estimate of the burn-weighted ion temperature, T_{ion}. The model also assumes that at stagnation Local Thermodynamic Equilibrium (LTE) conditions obtain, so the ion and electron temperatures are identical, $T_{ion} = T_e$.

Although the description above has focussed on the routinely available x-ray self-emission and nuclear data, other experimental fitting constraints may be added. For example, back-lit radiographic images are handled in a very similar fashion as the self-emission x-ray images:

ray-tracing is performed at the appropriate viewing angle using a constant attentuation factor

$$I_{rg}(x,y) = \exp\left(-0.304 \int_{path} \rho(z)\, dz\right) \tag{14}$$

for the radiographic image. The simulated image is again fit pointwise to the experimental image. Another valuable consistency constraint would be provided by high-resolution x-ray spectra of Ge that might have been mixed into the hot core. A ray-trace of the simulated emission would be fit pointwise to the experimental spectrum using the composition fraction of Ge and relative emission strength as fitting parameters. Interpolation on detailed atomic model tabular data in density and temperature thus produces a synthetic spectrum for the matching.

III. MODEL VALIDATION

Validation of the approach outlined above is of course crucial. Since many important quantities are not accessible experimentally, validation is best obtained by comparison to detailed radiation-hydrodynamic simulations. Also, in order to clarify the algorithmic aspect of the fitting procedure, the discussion below follows the fitting procedure as it is applied in typical circumstances. The specific case chosen here for validation purposes is a Revision 5 Symcap design with nominal, within specification, perturbations to the capsule[8]. The radiation-hydrodynamic code HYDRA[7] was used to simulate the imploding capsule and then post-processed to generate synthetic experimental data. Radiographic and x-ray self-emission images were calculated at their experimental positions. Finally, the DD neutron yield, 1.052×10^{11}, fuel composition, 0.07 atomic weight fraction of D, 0.93 atomic weight fraction of ^{3}He, and burn width, 173 ps, are given by the simulation. It should again be emphasized that the absolute intensities of the x-ray images are not used since these images are not typically absolutely calibrated. Similarly, the absolute calibration of the neutron time-of-flight signal is not generally known, hence is not used in the fit.

The fit to these combined data then proceeds by assuming values for the parameters appearing in the global fitting functions above with the inclusion of two overall x-ray self-emission scaling parameters, w_{norm} and p_{norm}, and one parameter that adjusts the minimum of the neutron time-of-flight signal, $ntof_m$. In the particular case under consideration, the set chosen was $b_{00}, c_{00}, c_{20}, c_{40}, d_{00}$, and of course a_1, a_2, and P for a total of 11 fitting parameters.

The initial choices $b_{00}, c_{00}, c_{20}, c_{40}, d_{00}, a_1$, and $a_{2,}$ generate the density on the grid; the value for P then produces the temperature at each point; opacity and emission are obtained from the density and temperature assuming an x-ray energy E of 9 keV; and the ray tracing then yields radiographic, polar and waist images. Next, density and temperature are evaluated pointwise in a sphere of radius 300 μm and the number of neutrons at each co-ordinate point is obtained and dispersed in energy using the Brysk expression. The neutron number is integrated over the sphere to produce the total neutron yield and the energy-dispersed spectrum is used to evaluate the neutron time-of-flight signal.

Standard least-squares fitting[9] is applied to obtain an optimized fit. In this particular example, there are three images (one radiograph and two orthogonal x-ray images) fit at each pixel (3× 41×41 points); the neutron time-of-flight signal is matched at each recorded time value near the voltage minimum (1200 points); and the neutron yield is fit (1 point). The eleven parameters are varied until the value of χ^2 is minimized. The optimized values are listed in Table I, and Table II contains the individual χ^2 values obtained. With these optimized fitting parameters, it is possible to derive a large number of "burn-weighted" (bw) quantities in the hot core. A comparison between the HYDRA values and those obtained from this fitting procedure are listed in Table III, along with the relative error in each quantity. The fitting parameter for the pressure relies upon the equation-of-state for a fixed THD mixture, hence the pressure for the different gas fill must be scaled by the appropriate gas mixture. The specific factor is $\frac{1}{2}\left(1+\sum_{1}^{n} Z_i f_i\right)$ for n species each with atomic number Z_i and atomic weight fraction f_i. The modified pressure value appears in Table III.

The agreement between the HYDRA quantities and those derived from the fit is reasonable. The fitting model does not distinguish between T_e and T_{ion} but a burn-weighted T_{ion}

Parameter	**Optimized Value**	**Fit Uncertainty**
a_1	12.50	0.54
a_2	73.40	2.64
b_{00}	0.7665	8.0e-2
c_{00}	7.71e-3	1.30e-4
c_{20}	-8.38e-5	7.79e-5
c_{40}	1.91e-4	7.58e-5
d_{00}	7.04e-4	1.10e-4
P	53.5	0.74
w_{norm}	0.998	8.0e-3
p_{norm}	2.36	2.0e-2
$ntof_m$	215.0	2.0e-2

TABLE I: Optimized fitting parameters and their associated uncertainities.

Fit Data	**Final χ^2value**
Radiograph	288
Waist x-ray	194
Polar x-ray	162
NTOF trace	20
Yield	0.11

TABLE II: Final χ^2 values from the fitting parameters in Table I.

comparable to the simulation is obtained from the full width-half-maximum of the energy-dispersed neutron signal. In this case, that value was 3.19 keV, in excellent agreement with the simulation result.

IV. EXPERIMENTAL ANALYSIS

As mentioned above, a substantial energy deficit is observed in the hot core internal energy when compared to radiation-hydrodynamic simulation. To elucidate this discrepancy more concretely, Table IV contains a detailed comparison of some specific values for a repre-

Implosion Metric	**Simulation**	**Fit**	**Relative Error**
$(\rho r)_{bw}\,(g/cm^2)$	0.0689	0.0625	-0.103
$(T_e)_{bw}\,(keV)$	3.16	3.42	7.54e-2
$(T_i)_{bw}\,(keV)$	3.20	3.42	6.5e-2
$(\rho_{ion})_{bw}\,(g/cm^3)$	23.87	23.96	3.45e-3
$(radius_{core})_{bw}\,(\mu m)$	33.1	37.1	0.101
$(mass)_{bw}\,(\mu g)$	18.91	20.20	6.4e-2
$(vol)_{bw}\,(\mu cm^3)$	6.45e-7	7.73e-7	0.165
$(n_e)_{bw}$	6.02e18	5.19e18	-0.16
$(\rho_e)_{bw}$	9.33e24	6.72e24	-0.389
$(PV)_{bw}\,(J)$	4.42e3	4.48e3	1.35e-2
$\left(\frac{3}{2}kT\right)_{bw}(J)$	6.54e3	6.48e3	-9.6e-3
$radius_{waist}(0.18)(\mu m)$	50.3	50.3	-
$radius_{pole}(0.18)(\mu m)$	47.8	50.3	4.94e-2
$P\,(Gbar)$	69.8	58.0	-0.204
DD n-$Yield$	1.05e11	1.07e11	1.3e-2

TABLE III: Various derived quantities from the optimized fit. Note that pressure in this table differs from the fitting parameter pressure by a factor that compensates for the composition of the gas. The waist and pole radii are those at a contour value of 0.17 of the respective maximum values.

sentative cryogenic DT-filled capsule implosion on the NIF – shot N120321. This particular shot is interesting since it demonstrated several favorable characteristics: large DSR, relatively high yield, and generally round x-ray images. The otherwise nominal capsule had twice the amount of Silicon dopant compared to previous shots; a depleted Uranium layer formed the inner wall of the hohlraum; and the 320 TW laser pulse had an extended fourth pulse. The radiation-hydrodynamic values are derived from a post-shot simulation that attempts to match the experimental DSR, T_{ion}, and 13-15 MeV neutron yield[10]. Correlated fitting of the experimental stagnation properties using the three-dimensional isobaric model produced the values listed. This comparison highlights the typical trend seen in the cryogenic DT experiments, namely the reduced burn volume and pressure that imply reduced

N120321	**Experiment**	**Post-shot Simulation**	**Correlated Fit**
$Yield(13-15MeV)$	4.20e14	2.40e15	4.00e14
$(T_i)_{bw}\,(keV)_{ntof}$	2.99	3.16	3.00
DSR	0.062	0.072	0.059
$\rho r_{fuel}\,(g/cm^2)$	1.30	1.51	1.24
$radius_{waist}(0.17)(\mu m)$	16	19	21
$radius_{pole}(0.17)(\mu m)$	23	20	21
$(mass)_{bw}\,(\mu g)$		13.2	3.7
$(vol)_{bw}\,(\mu cm^3)$		1.24e-7	0.73e-7
$P\,(Gbar)$		256	110
$\left(\frac{3}{2}PV\right)_{fuel}(kJ)$		10.86	6.7 $\pm$0.5
$\left(\frac{3}{2}PV\right)_{hs}(kJ)$		4.76	1.2 $\pm$1.0

TABLE IV: Comparison of experimental data, post-shot simulation, and the results of the model fit for shot N120321.

hot spot internal energy. It is noteworthy that the post-shot simulation matches several experimental quantities reasonably well, especially the burn-weighted ion temperature, DSR, and x-ray self-emission image radii yet the neutron yield differs by a factor of four. This disagreement underscores the importance of matching all stagnation properties rather than a subset.

Nuclear diagnostic information can be derived from the integrated fitting procedure by three-dimensional imbedding of the model parameters in HYDRA and performing high-fidelity Monte Carlo neutron transport calculations. Using this technique, the variation in DSR values along different lines of sight are found to induce equatorial asymmetries in the fit of the DT fuel assembly. The so-called SpecA NTOF (Alcove Spectrometer) at (116,316), and SpecE NTOF (Equatorial Spectrometer) at (90,174), DSR determinations vary for the majority of the cryogenic DT implosion experiments. The ratio of these two DSR values is plotted in Figure 3 as a function of shot date. The SpecE DSR is typically lower than the SpecA DSR indicating an excess of high density DT in the SpecA direction. Fitting the

nTOF	**Experiment**	**Fit**
$SpecA\,(116, 316)$	0.067	0.064
$SpecE\,(90, 174)$	0.051	0.057
$MRS\,(77, 324)$	0.070	0.066
$NITOF\,(90, 315)$	0.063	0.062

TABLE V: Comparison of the experimental line-of-sight DSR data for shot N120321 with the model fit determination.

fuel shell density for the four NTOF diagnostics from shot N120321 produces a pronounced asymmetry in the resulting mass distribution as depicted in Figures 4 and 5 for two different cross-sectional views of the fuel assembly. The individual DSR values for each of these NTOF's are given in Table V.

Other important nuclear diagnostic information is derived from the Monte Carlo neutron transport calculations. Pinhole images of neutrons in any desired energy range may be calculated and compared to the experimental images[11]. The N120321 experimental pinhole image for neutrons with energy between 13-17 MeV is displayed in the left-most plot of Figure 6 and in the middle plot for neutron energies between 6-12 MeV. The higher energy range image reveals the spatial extent of the burning region whereas the lower energy range image tracks the scattered neutrons and thus the cold fuel assembly. By superimposing these two images and reducing the intensity scale of the higher energy image, a more suggestive picture of the cold fuel assembly appears as shown in the right-most plot in Figure 6. Although the two separate pinhole images do not display significant asymmetry, the overlaid image does. The analogous images derived from the fitting procedure are shown in Figure 7 along with the corresponding overlaid image, which clearly displays the fuel asymmetry. The higher neutron energy images are reasonably similar but the lower neutron energy images disagree in size and symmetry. This discrepancy is not understood at present although some tentative explanations have been advanced[11].

Further correspondence with directional nuclear data can be made by matching the Nuclear Activation Diagnostic (NAD) values[12]. This diagnostic consists of Zr foils (for DT implosions) mounted on some of the NIF target chamber flanges and are activated by the resulting neutron flux. The specific activation reaction for cryogenic DT-filled capsules is

^{90}Zr(n,2n)^{89}Zr which has an energy threshold of about 12 MeV. Thus the observed activation is only sensitive to the unscattered neutrons. Relative variations in activation at different flange sites indicate the relative fuel areal density variations. For example, if a particular site has higher activation than a reference activated foil, then there was correspondingly less areal density in that line of sight. A polar map of these relative activations for N120321 is displayed in Figure 7 which qualitatively shows more mass along the polar directions than along the equatorial directions. Reasonable agreement with the derived fit to this experiment is obtained, as demonstrated by the analogous polar plot in Figure 8.

V. CONCLUSION

The proposed model attempts to correlate disparate experimental data using a simple phyiscal description of the imploded capsule. In the absence of detailed, calibrated experimental data, validation of the model relies upon a stringent comparison to radiation hydrodynamic code simulation which supplies some confidence that the basic assumptions and methodology are sound. In addition to fitting extant data, this model could also be used in a predictive sense to estimate the ignition margin. For example, after successful fitting of a fielded THD capsule, the gas fill could be changed to DT thereby obtaining an estimate for the expected neutron yield.

A few important limitations of the procedure should be noted. First, it is quite difficult to quantitatively estimate the error and consequent reliability of the fits. Both experimental uncertainties and numerical fitting errors combine to make any error propagation analysis suspect. The validation procedure again provides some guidance on this issue but the quoted uncertainities are likely to be optimistic. Second, the presence of high velocity material "jets" might produce pressure gradients at stagnation, thereby invalidating, or at least complicating, the use of an isobaric approximation. Large pressure gradients are sometimes observed in hydrodynamic simulations with large laser drive asymmetries. Third, the composition of the hot core is assumed to be known. This assumption would of course fail in the presence of ablator shell mix. That is, if a substantial amount of shell material is dynamically introduced into the hot core, then the x-ray self-emission images might be misleading due to anomalously high emission brightness due to Carbon in the hot core. The apparent image size will appear to decrease, as measured by the 0.17 maximum contour level, skew-

ing the fit to smaller volume and higher pressure. On the other hand, differential filtering, such as the use of Ross pair filters, or including the high resolution spectroscopic data from dopants such as Ge into the fit might resolve this problem. Fourth, the determination of the compressed, colder shell is unreliable without a radiographic image to directly constrain the fit in this region. It might be possible to address this deficiency using data from the convergent mass ablation diagnostic but a dynamic model is required to link the peak implosion velocity capsule characteristics to the stagnated shell final state. Ongoing research is directed toward this goal[13]. Presently the indirect approach of correlating nuclear and x-ray diagnostic information described above is the only means available to address this issue.

VI. ACKNOWLEDGMENTS

The authors would like to thank many scientists for their assistance. J. Caggiano, J. Knauer, J. McNaney, and M. Moran supplied the high quality NTOF data. D. Munro was our primary source for the NTOF Instrumental Response Functions. G. Kyrala, S. Glenn, N. Izumi, and T. Ma provided valuable guidance on the x-ray self-emission images. D. Clark, O. Jones, R. Town and S. Weber generously shared their detailed radiation-hydrodynamic simulations. R. Betti and M. Key supplied useful critical commentary on the limitations of the model procedure. P. Patel provided the plots in Figures 1, 2 and 3. This work was performed under the auspices of the U. S. Department of Energy by the Lawrence Livermore National Laboratory under Contract DE-AC52-07NA27344.

VII. REFERENCES

[1] M. C. Herrmann., M. Tabak, J. D. Lindl, Nucl. Fusion, **41**, 99(2001); J. Meyer-ter-Vehn, Nucl. Fusion, **22**, 5619(1982); M. D. Rosen, J. D. Lindl, A. R. Thiessen, Laser Programs Annual Report – 1983, Lawrence Livermore National Laboratory, CA Chp. 3, pg. 5 (1984); V. A. Smalyuk, J. A. Delettrez, S. B. Dumanis, R. Epstein, V. Yu. Glebov, D. D. Meyerhofer, P. B. Radha, S. P. Regan, T. C. Sangster,C. Stoeckl, N. C. Toscano, J. A. Frenje, C. K. Li, R. D.

Petrasso, F. H. Seguin and J. A. Koch, Phys. Plasmas, **12**, 052706 (2005); V. A. Smalyuk, S. B. Dumanis, J. A. Delettrez, V. Yu. Glebov, D. D. Meyerhofer, S. P. Regan, T. C. Sangster, and C. Stoeckl, Phys. Plasmas, **13**, 104502 (2006).

[2] S. Atzeni, and J. Meyer-ter-Vehn, "The Physics of Inertial Fusion", Section 10.6.3, (Clarendon Press, Oxford, 2004).

[3] G. R. Coughlan and W. A. Fowler, Atomic Nucl. Data, **40**, 283(1988).

[4] Multiple simulations under many conditions produce a proportionality constant of 21. (B. Spears, private communication).

[5] Report on the Los Alamos Equation-of-State Library. T-4 group, Los Alamos National Laboratory, Los Alamos, N. M. Report LALP-83-4.

[6] H. Brysk, Plasma Physics, **15,** 611(1973).

[7] M. M. Marinak, G. D. Kerbel, N. A. Gentile, O. Jones, D. Munro, S. Pollaine, T. R. Dittrich, and S. Haan, Phys. Plasmas, **8**, 2275(2001).

[8] S. W. Haan, J. D. Lindl, D. A. Callahan, D. S. Clark, J. D. Salmonson, B. A. Hammel, L. J. Atherton, R. C. Cook, M. J. Edwards, G. Glenzer, A. V. Hamza, S. P. Hatchett, M. C. Herrmann, D. E. Hinkel, D. D. Ho, H. Huang, O. S. Jones, J. Kline, G. Kyrala, O. L. Landen, B. J. MacGowan, M. M. Marinak, D. D. Meyerhofer, J. L. Milovich, K. A. Moreno, E. I. Moses, D. H. Munro, A. Nikroo, R. E. Olson, K. Peterson, S. M. Pollaine, J. E. Ralph, H. F. Robey, B. K. Spears, P. T. Springer, L. J. Suter, C. A. Thomas, R. P. Town, R. Vesey, S. V. Weber, H. L. Wilkens, and D. C. Wilson, Phys. Plasmas, **18**, 051001 (2011).

[9] W. H. Press, B. P. Flannery, S. A. Teukolsky, and W. T. Vetterling, "Numerical Recipes", Section 14.3, (Cambridge University Press, Cambridge, 1986).

[10] D. Clark, DPP presentation BI3.00001.

[11] G. Grim, DPP presentation BI3.00003.

[12] D. L. Bleuel, C. B. Yeamans, L. A. Bernstein, R. M. Bionta, J. A. Caggiano, D. T. Casey, G. W. Cooper, O. B. Drury, J. A. Frenje, C. A. Hagmann, R. Hatarik, J. P. Knauer, M. Gatu Johnson, K. M. Knittel, R. J. Leeper, J. M. McNaney, M. Moran, C. L. Ruiz, and D. H. G. Schneider, Rev. Sci. Inst. **83**, 10D313(2012).

[13] R. Betti, K. Anderson, V. N. Goncharov, R. L. McCrory, D. D. Meyerhofer, S. Skupsky, and R. P. J. Town, Phys. Plasmas, 9, 2277(2002); K. Anderson and R. Betti, Phys. Plasmas, **10**, 4448(2003).

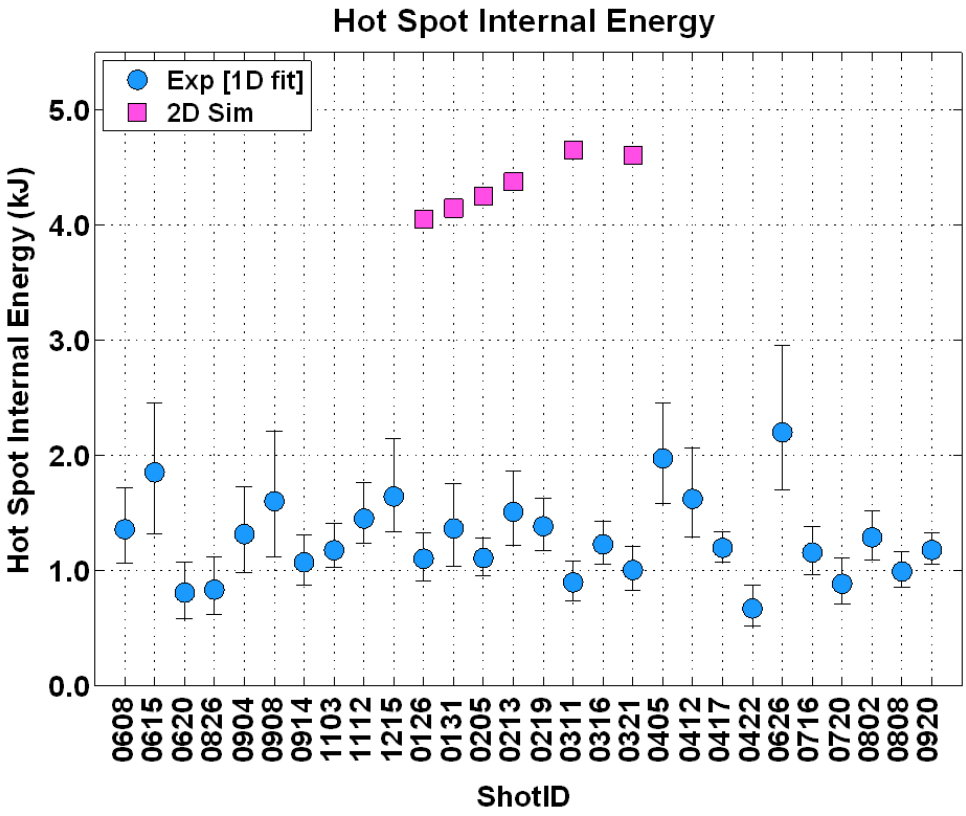

FIG. 1: The internal energy deficit between experimentally derived values and selected HYDRA simulations is plotted as a function of chronological shot number.

VIII. FIGURES

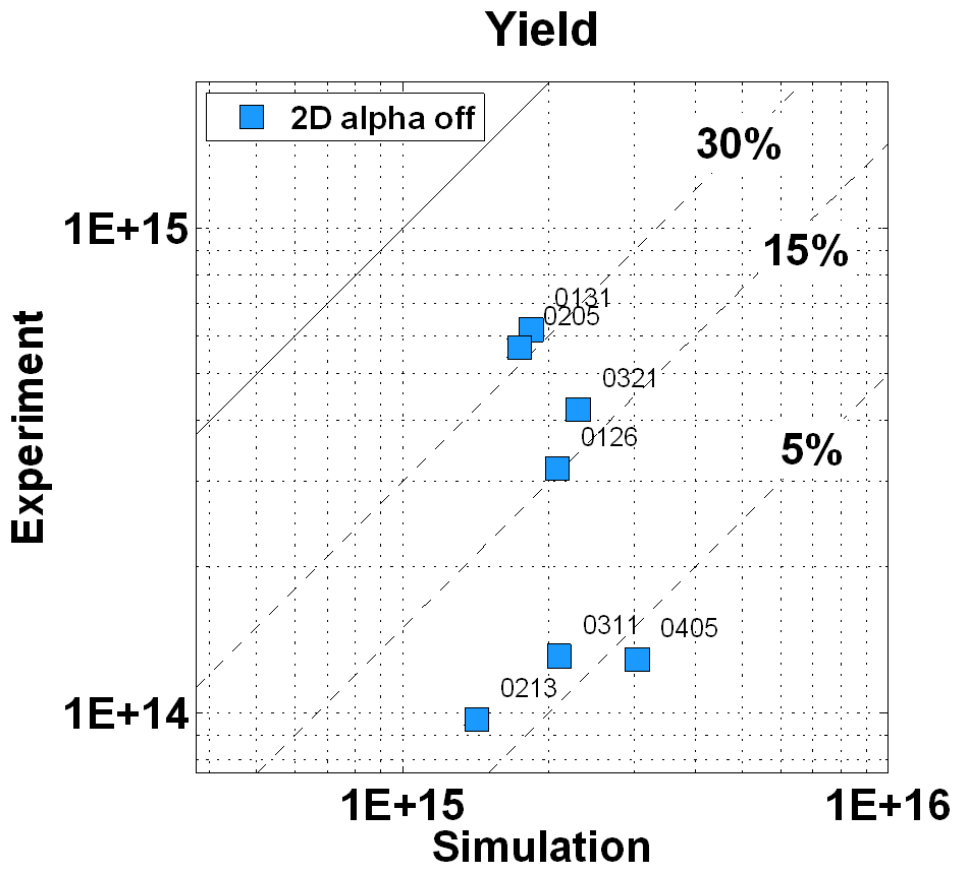

FIG. 2: The experimental yield is plotted against the HYDRA simulated yield for selected shots displaying typical disagreement.

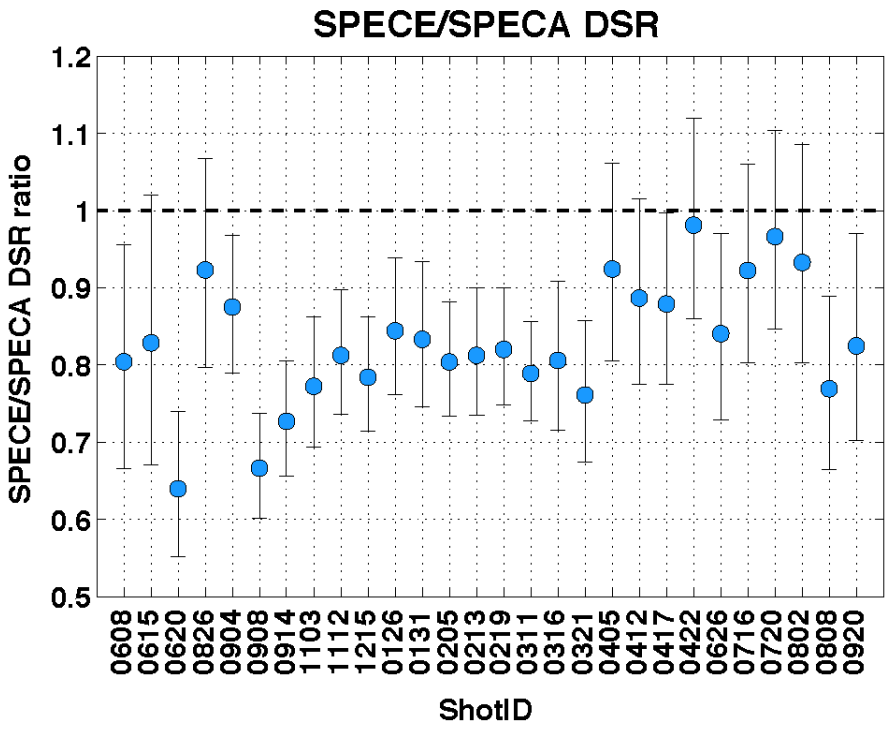

FIG. 3: The variation in the ratio of the SpecE to SpecA DSR measurement plotted as a function of chronological shot number.

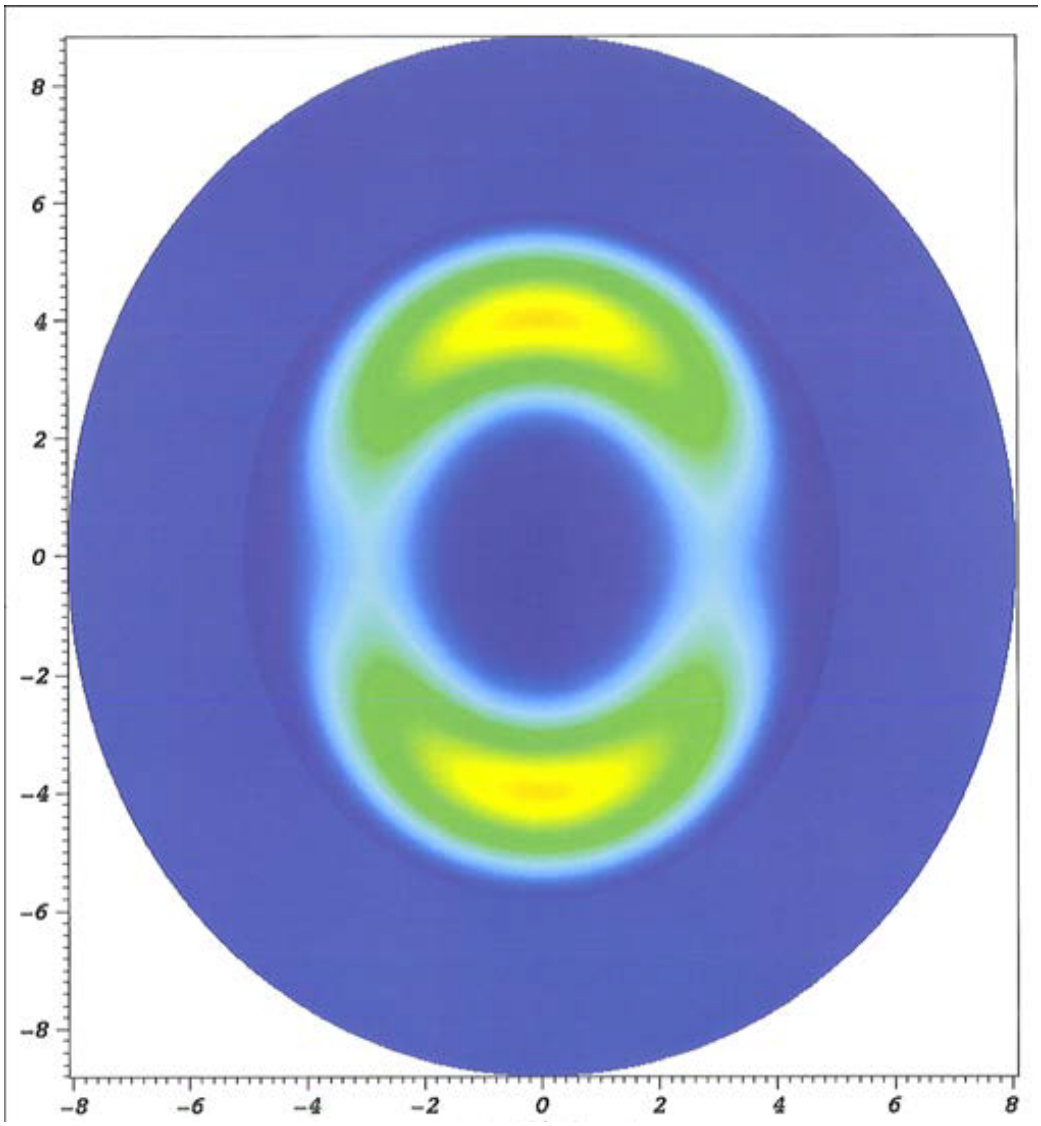

FIG. 4: The derived density distribution for shot N120321 is plotted in the (y,z) plane, dipslaying polar cap asymmetry.

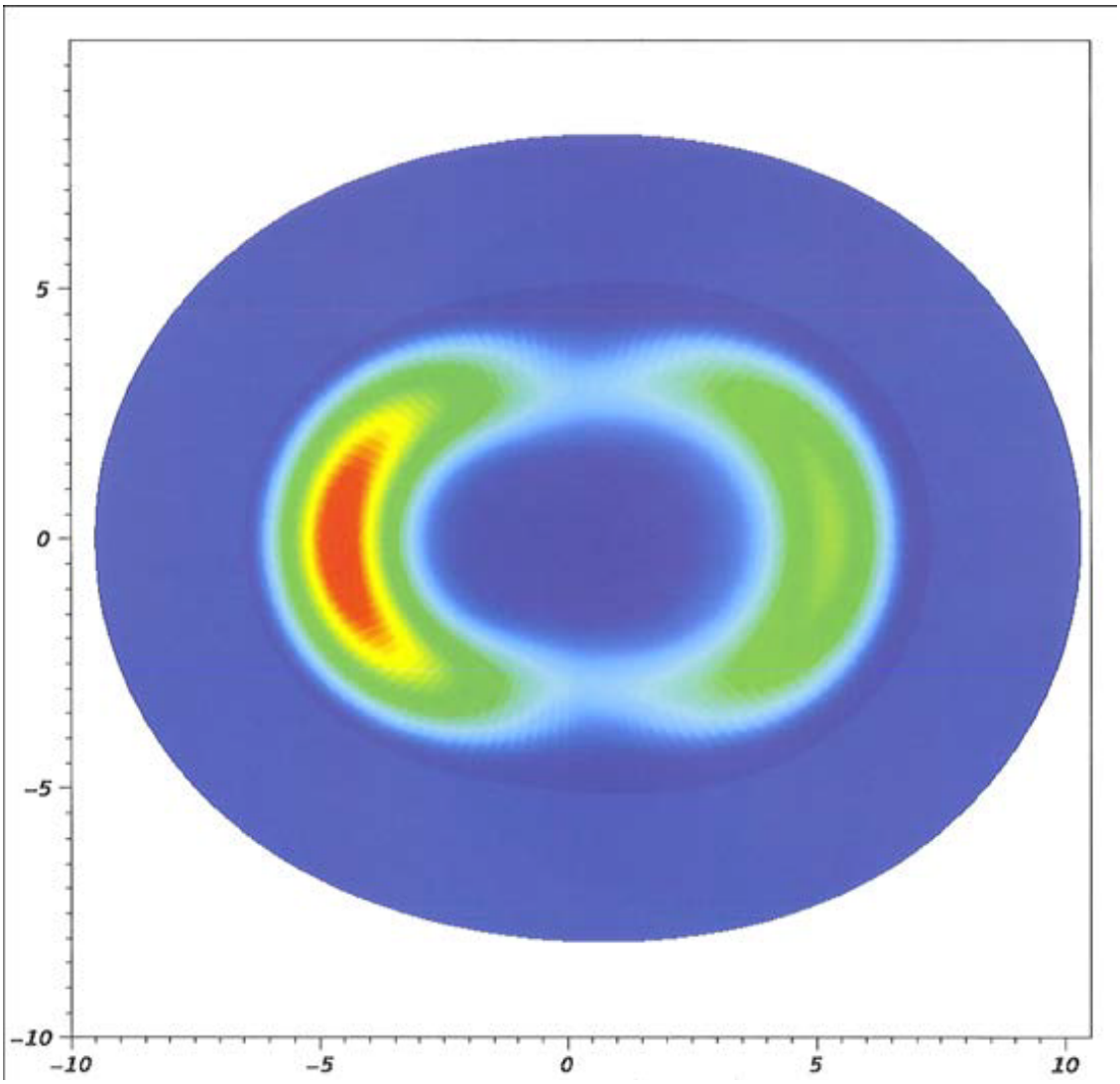

FIG. 5: The derived density distribution for shot N120321 is plotted in the (x,y) plane, displaying sizeable equatorial asymmetry.

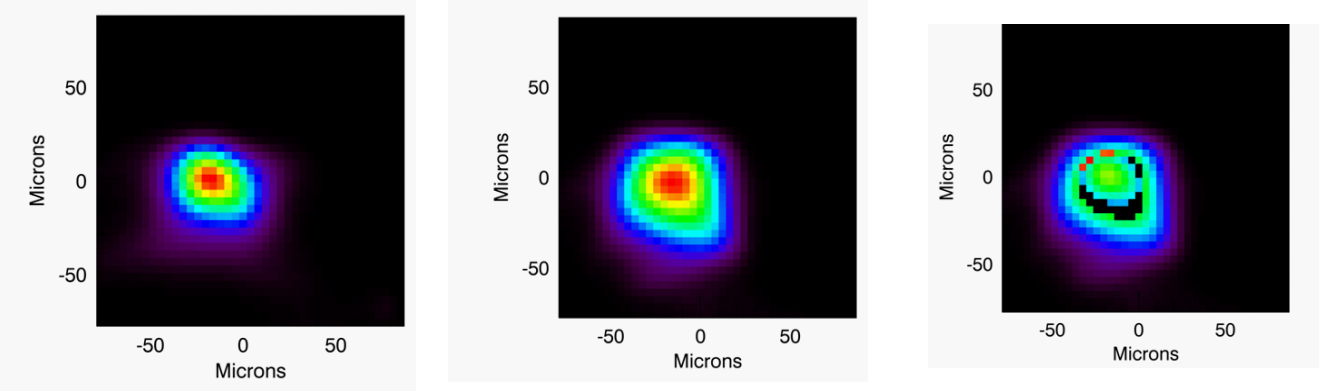

FIG. 6: The experimental neutron images in the energy range 13-15 MeV, 6-12 MeV, and the overlaid image, respectively.

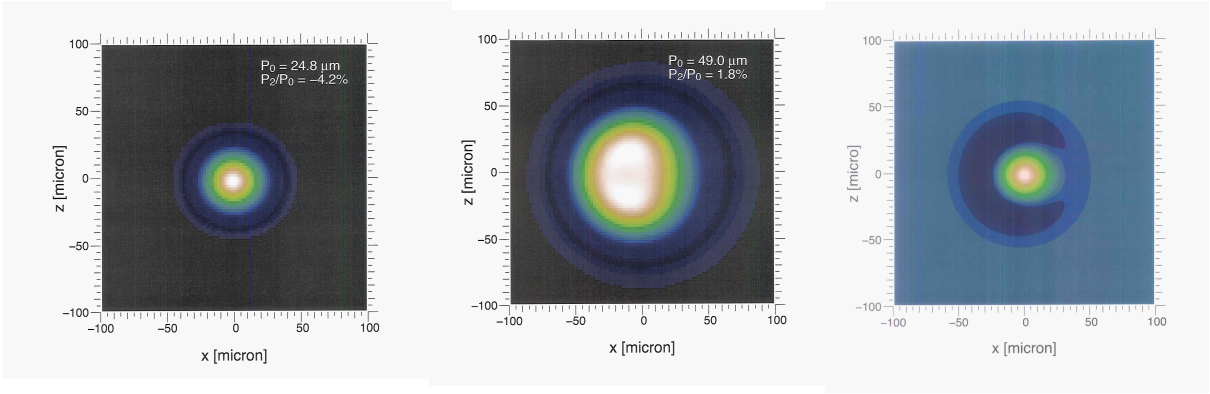

FIG. 7: The fit neutron images in the energy range 13-15 MeV, 6-12 MeV, and the overlaid image, respectively.

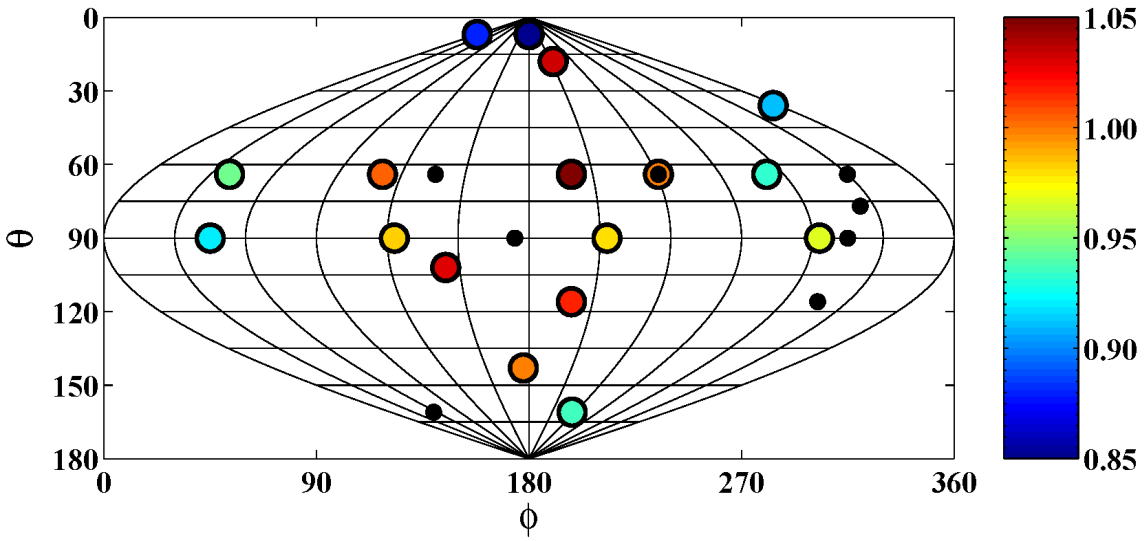

FIG. 8: Experimental distribution of Zr activation ratios plotted in (θ, ϕ) .The black markers correspond to existing non-activation nuclear diagnostic experiments; the superimposed black marker and colored circle represents the NAD site used to calibrate the Alcove NTOF.

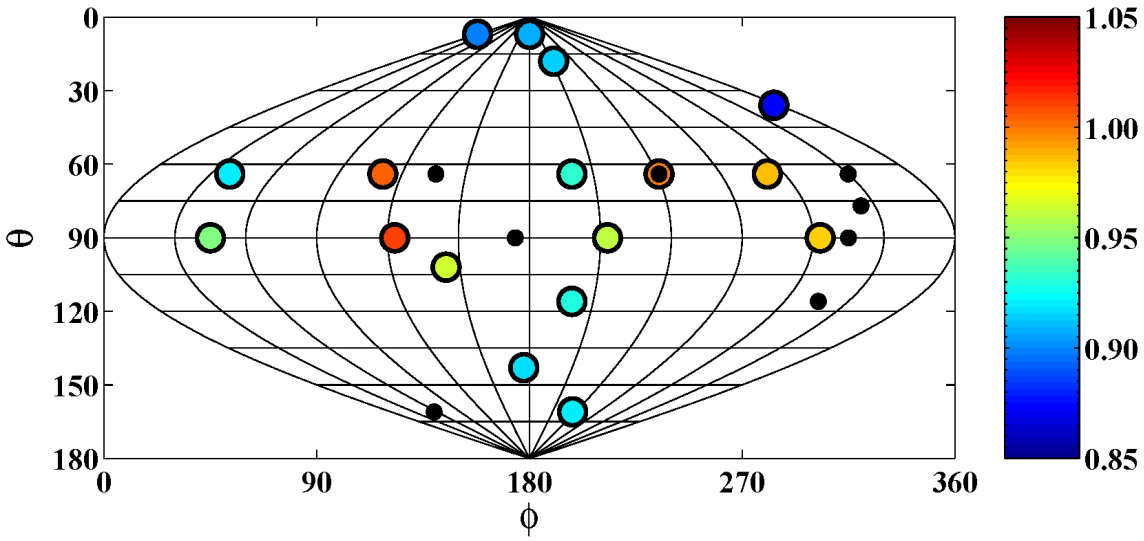

FIG. 9: Fit distribution of Zr activation ratios plotted in (θ, ϕ) .The marker and circle choice is identical to that of Figure 8.